ELSEVIER

Contents lists available at ScienceDirect

### Earth and Planetary Science Letters

journal homepage: www.elsevier.com/locate/epsl





## Fluids control along-strike variations in the Alaska megathrust slip

Fan Wang <sup>a,\*</sup>, S. Shawn Wei <sup>a,\*</sup>, Connor Drooff <sup>a</sup>, Julie L. Elliott <sup>a</sup>, Jeffrey T. Freymueller <sup>a</sup>, Natalia A. Ruppert <sup>b</sup>, Haijiang Zhang <sup>c</sup>

- <sup>a</sup> Department of Earth and Environmental Sciences, Michigan State University, East Lansing, MI, USA
- <sup>b</sup> Alaska Earthquake Center, University of Alaska Fairbanks, Fairbanks, AK, USA
- <sup>c</sup> School of Earth and Space Sciences, University of Science and Technology of China, Hefei, Anhui, China

#### ARTICLE INFO

#### Keywords: Subduction zone Alaska peninsula Body-wave tomography Slip behavior Fluids Megathrust earthquakes

#### ABSTRACT

Interseismic and coseismic slip on the subduction zone megathrust show complex along-strike variations and the controlling factors remain debated. Here we image seismic velocity anomalies to infer fluid distribution in the Alaska subduction zone (Alaska Peninsula section) with seismic tomography. The weakly locked Shumagin segment is characterized by abundant fluids on the plate interface and in the overriding plate, whereas the moderately-to-highly locked Chignik and Chirikof segments that hosted M>8 earthquakes are relatively dry. The Kodiak segment, which was ruptured by the 1964 M9.2 Great Alaska earthquake and is presently fully locked near the trench, is characterized by a fluid-rich plate interface but a fluid-poor and inferred low-porosity overriding plate. Multiple large earthquakes have nucleated in fluid-rich regions at the plate interface. Our study highlights the important roles of fluids, particularly in the overriding plate, in controlling interseismic slip deficit and earthquake rupture. We propose that a fluid-rich overriding plate means that there has been a high sustained flux of fluids across the plate interface, which enhances the formation of clay minerals that promote fault creep.

#### 1. Introduction

Almost all great earthquakes (M > 8) occur on megathrust faults in subduction zones. Previous observations and simulations focus on the plate interface and subducted plate and suggest that varying roughness, sediment thickness, and fluids at the plate interface may cause different slip behaviors, ranging from aseismic slip to megathrust earthquakes (Audet et al., 2009; Guo et al., 2021; Heise et al., 2017; Kodaira et al., 2004; Lay et al., 2012; Li et al., 2018a; Moreno et al., 2014; Shillington et al., 2015; Sun et al., 2020). Specifically, fluids released from sediment compaction and metamorphic dehydration reactions of hydrous minerals in the subducted slab play a critical role in controlling the stress state and frictional properties along the megathrust (Saffer and Tobin, 2011; Tobin and Saffer, 2009). These fluids can be either trapped at the plate interface or released into the overriding plate. The porosity of the overriding plate thus depends on not only the fluid supply from slab dehydration but also the permeability and evolution history of the materials overlying the megathrust. Although a classic depth-dependent model focusing on fluid conditions at the plate interface (Lay et al., 2012; Saffer and Tobin, 2011) can well explain seismic and aseismic activities in the Nankai subduction zone, more complexities have been observed in other subduction margins (Nishikawa et al., 2019). In recent years, properties of the overriding plate in the forearc region, including its lithology, porosity, and rigidity, have received increasing attention as controlling factors of megathrust slip behavior and the earthquake rupture process (Arnulf et al., 2022; Bassett et al., 2016, 2014; Chesley et al., 2021; Egbert et al., 2022; Sallares and Ranero, 2019; Shillington et al., 2022). However, questions remain on which factor or factors dominate the interseismic and coseismic slip behaviors. A comprehensive investigation of a single subduction zone with earthquake and slip features that vary along strike is needed to understand the controlling factors of slip behaviors and their influence on large megathrust earthquakes.

The Alaska Peninsula section of the Alaska-Aleutian subduction zone displays complex along-strike variations in interseismic slip behavior and crustal and mantle structures, providing an ideal natural laboratory to study slip behaviors on the megathrust (Cordell et al., 2023; Drooff and Freymueller, 2021; Li et al., 2018a; Liu et al., 2022a; Lynner, 2021; Shillington et al., 2015; Wei et al., 2021; Xiao et al., 2021). We identify four along-strike segments from southwest to northeast based on the

E-mail addresses: wangfa16@msu.edu (F. Wang), swei@msu.edu (S.S. Wei).

<sup>\*</sup> Corresponding authors.

seismic and geodetic observations in this study (Fig. 1): Shumagin, Chignik, Chirikof, and Kodiak. Although the region between the Shumagin and Kodiak islands was conventionally referred to as the "Semidi" segment (e.g., Shillington et al., 2022), we divide it into the Chignik and Chirikof segments along a trench-normal boundary crossing the Semidi Islands, because these two segments exhibit distinct characteristics from our seismic tomography images and geodetic modeling. The most recent megathrust earthquakes, the 2020 M7.8 Simeonof and 2021 M8.2 Chignik events, ruptured two close-spaced segments that show distinct differences in interseismic coupling (Davies et al., 1981; Drooff and Freymueller, 2021; Elliott et al., 2022; Xiao et al., 2021) (Fig. 1), which shows that interseismic coupling alone cannot predict seismic hazard. In this region, the Pacific Plate subducts beneath the North American Plate at a convergence rate of ~6.3 cm/yr in a nearly trench-normal direction (Argus et al., 2010). Interseismic geodetic observations indicate that the subducted slab and the overriding plate are fully locked together outboard of Kodiak Island, whereas the megathrust slip transitions to weak locking outboard of the Shumagin Islands (Drooff and Freymueller, 2021; Xiao et al., 2021). It is worth noting that a region of low or no frictional locking adjacent to a fully frictionally locked region may still exhibit a high interseismic slip deficit due to the stress shadow effect (Lindsey et al., 2021; Zhao et al., 2022a). Therefore, we use slip deficit instead of plate locking to describe the geodetic constraints on interseismic slip behavior in the rest of this study. In addition to the 1964 M9.2 Great Alaska earthquake that ruptured the high-slip-deficit Kodiak segment, large megathrust earthquakes have occurred every ~50-75 years in the nearby Chignik segment where a high slip deficit is also observed (Davies et al., 1981; Li et al., 2018a; Ye et al., 2021) (Fig. 1). The most recent 2021 M8.2 Chignik earthquake mostly ruptures the 20-to 40-km depth of the plate interface within the Chignik segment. In contrast, the Shumagin segment with a low slip deficit did not rupture in a great megathrust earthquake for at least 200 years prior to the 2020 M7.8 Simeonof earthquake (Elliott et al., 2022; Witter et al., 2014; Ye et al., 2021).

What causes these along-strike changes despite the uniform convergence rate and direction? One possible answer is that the incoming plate exhibits along-strike changes. The pre-existing seafloor fabric and normal faults in the Pacific Plate have a low angle with the trench to the southwest in the Shumagin segment, while their orientations are nearly perpendicular to the trench to the northeast in the Chirikof and Kodiak segments (Shillington et al., 2015) (Figs. 1, 4). Consequently, more bending faults are re-activated at the outer rise, and thus the incoming plate is likely to be more hydrated in the Shumagin segment than in the neighboring Chignik segment. The Shumagin segment has a thin sediment layer being subducted, whereas thick sediments are present in the Chignik, Chirikof, and Kodiak segments due to the subduction of the Zodiac and Surveyor sedimentary fans (Li et al., 2018a). Given these systematic along-strike changes, Shillington et al. (2015) hypothesized that changes in the hydration state of the incoming lithosphere may control interseismic plate coupling and megathrust earthquake potential in the Alaska Peninsula through the volume of subducted fluids. On the other hand, the changes in the overriding plate crust properties may also influence megathrust earthquakes in this region (Shillington et al., 2022). In addition, a recent electromagnetic

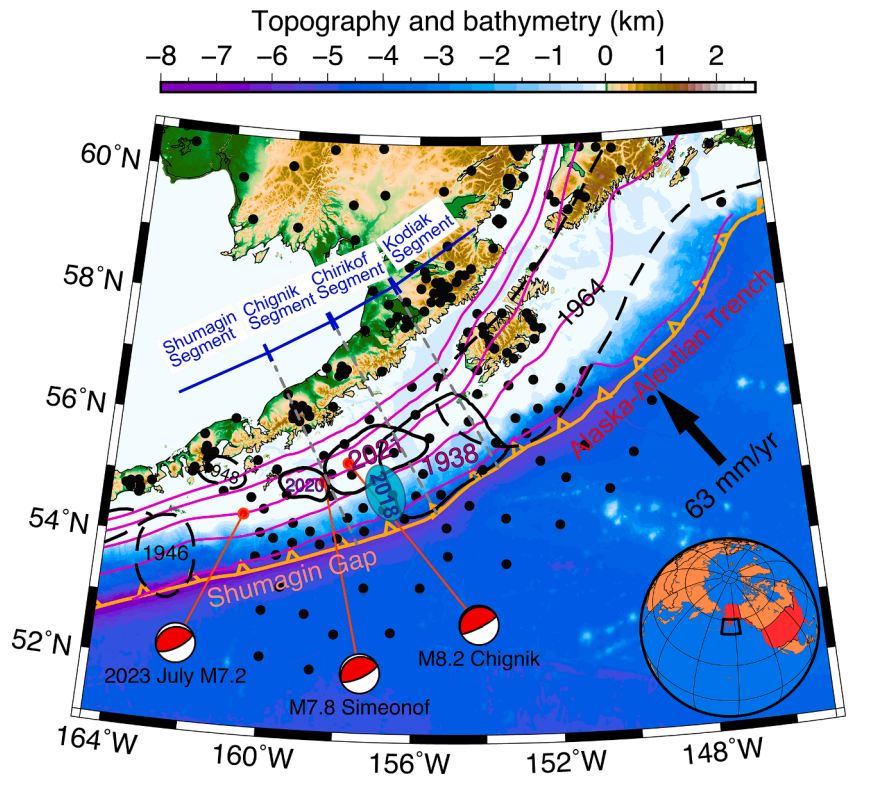


Fig. 1. Topography and bathymetry map of the Alaska Peninsula and adjacent regions. The new along-strike segmentation of the megathrust is determined based on the seismic tomography and plate coupling models in this study. Note that we avoid using "Semidi segment", a term commonly used in previous studies (Li et al., 2018a; Lynner, 2021; Shillington et al., 2015; Wei et al., 2021), because the Semidi Islands lie on the boundary between the Chignik and Chirikof segments. Dark black circles are seismic stations used in this study (Fig. 2c). The magenta curves illustrate the slab surface (top of the plate interface) at 10, 20, 30, 40, and 50 km depths. The slab surface geometry is based on a model constrained by active-source seismic experiments (Kuehn, 2019) in addition to the Slab2 model (Hayes et al., 2018). Black dashed contours outline the rupture zones of historical megathrust earthquakes determined from their aftershock distributions (Davies et al., 1981). Black solid contours show 1-m slip areas of previous megathrust earthquakes whose finite slip models have been recently determined by Freymueller et al. (2021), Xiao et al. (2021) and Elliott et al. (2022). Cyan-shaded ellipse shows the preferred area of a slow slip event in 2018 reported by He et al. (2023). Red-filled beachballs indicate the Global CMT focal mechanisms (Ekström et al., 2012) and hypocenters of the 2020 M7.8 Simeonof, 2021 M8.2 Chignik, and 2023 July M7.2 Sand Point megathrust earthquakes.

study suggests that the weak plate coupling in the Shumagin segment does not solely result from fluids (Cordell et al., 2023). Yet the details of the controlling factors remain unclear due to the lack of 3D images of the megathrust and overriding plate in this region.

In this study, we utilize a seismic body-wave double-difference tomography technique to construct a 3D high-resolution velocity structure of the Alaska Peninsula. We also develop a new slip deficit model based on continuous and campaign GNSS measurements, independent from our seismic imaging. Furthermore, we investigate the structural variations of the overriding plate and the plate interface in different segments along the strike, and their relationships with interseismic slip deficit.

#### 2. Data and methods

#### 2.1. Seismic travel-time tomography

In this study, we image the high-resolution 3D seismic velocity structure of the Alaska Peninsula and the adjacent regions using body-wave travel-time data recorded by the Alaska Amphibious Community Seismic Experiment (AACSE) and the adjacent stations of the EarthScope Transportable Array and the Alaska Earthquake Center (Ruppert et al., 2022) (Fig. 2). AACSE ocean-bottom seismographs (OBSs) in the outer

rise and fore-arc regions provide critical data for high-resolution images of the megathrust, which is mainly offshore. We conduct a body-wave travel-time tomographic imaging on multiple scales. First, we develop a large-scale velocity model using regional and teleseismic data. Second, we use this model as a starting model to image the  $V_P$  and  $V_P/V_S$  structure down to 200 km depth with only regional seismic data. With this strategy, our final results are largely independent of the starting model (Fig. 3).

In the first step, we assemble the P- and S-wave arrival times from May 2018 through August 2019 recorded by onshore and offshore seismic stations of the AACSE, EarthScope USArray, and the Alaska regional network (Fig. 2c), as well as teleseismic traveltime data of Alaskan earthquakes recorded by global stations and global events recorded by Alaskan stations. We use an improved version of teletomoDD (Pesicek et al., 2014), a teleseismic double-difference tomography package, to invert the regional and teleseismic arrival times for 3-D  $V_P$  and  $V_S$  models down to 700 km depth. The starting velocity model is constructed by combining the top 50 km part of a recent regional  $V_S$  model constrained by ambient noise and teleseismic surface waves (Li et al., 2024) and a 3D global model TX2019slab below 50 km depth. We perform four iterations of joint inversion for velocity and relocation and two iterations of inversion for only relocation.

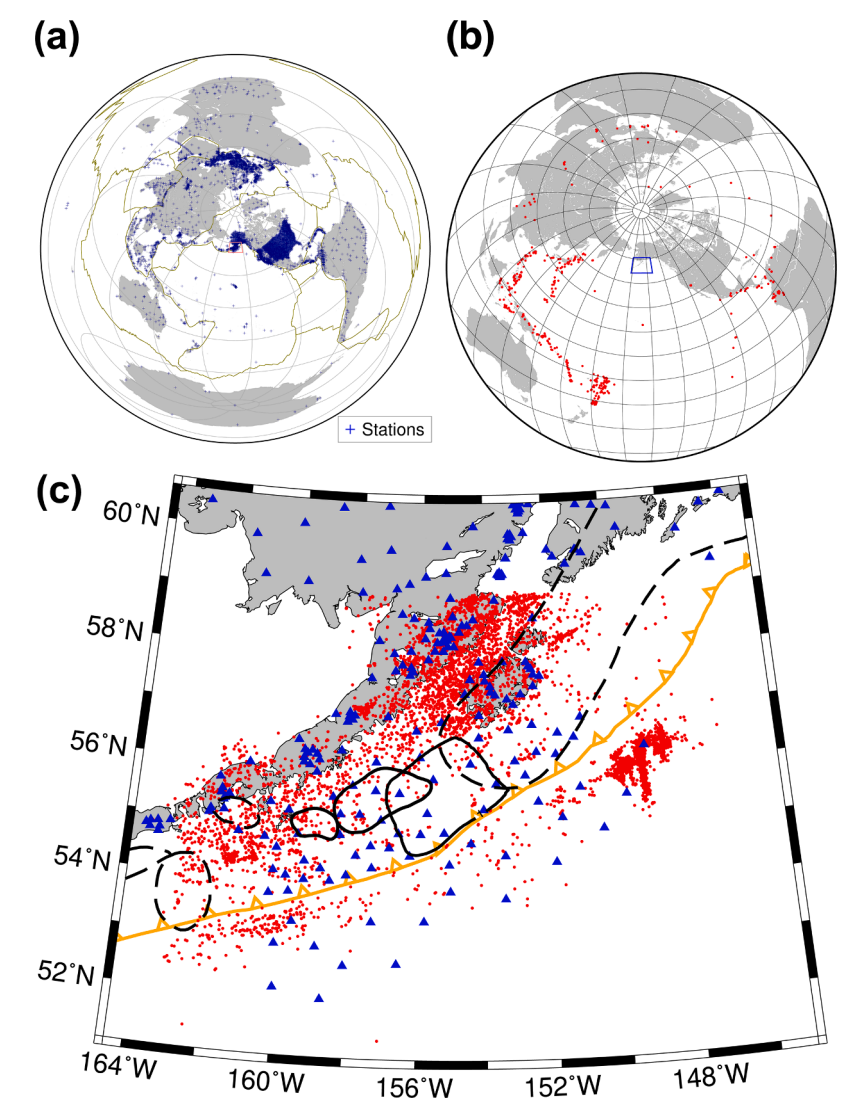


Fig. 2. Event and station distributions used in this study. Distribution of global stations (a) and teleseismic events (b) are used in the first step of tomography for a large-scale velocity model. (c) Distribution of regional stations (blue triangles) and local events (red dots) used in the second step of tomography for high-resolution  $V_P$  and  $V_P/V_S$  models. Other features are the same as in Fig. 1.

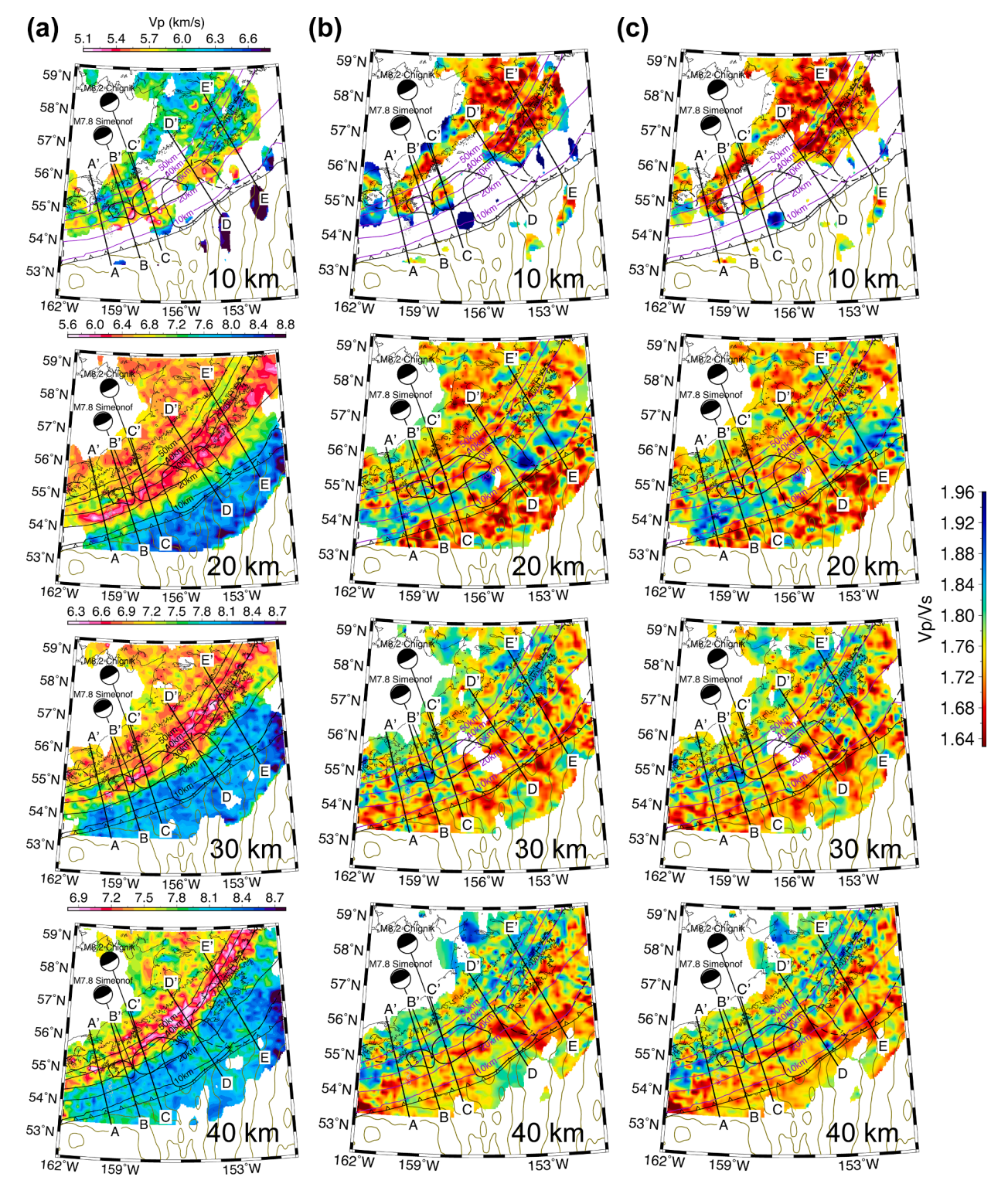


Fig. 3. Maps of  $V_P$  and  $V_P/V_S$  models using different starting  $V_P/V_S$  values at constant depths of 10, 20, 30, and 40 km. (a) Final  $V_P$  model. (b)  $V_P/V_S$  model inverted using the  $V_P/V_S$  values from the first step as the starting model. (c) Final  $V_P/V_S$  model inverted using a uniform value of 1.75 as the starting model. Bold black lines indicate the cross-sections in Figs. 5 and 6. Other features are the same as in Fig. 1.

In the second step, we invert for higher-resolution  $V_P$  and  $V_P/V_S$  models from 0 to 200 km depths using only regional seismic data, using two sets of starting models, and a new version of tomoDD (Guo et al., 2018; Zhang and Thurber, 2003) that can simultaneously determine  $V_P$ ,  $V_S$ , and  $V_P/V_S$  models using P, S, and S-P arrival times. The first starting  $V_P$  and  $V_P/V_S$  models directly come from the first step. However, because the  $V_P$  and  $V_S$  models from the first step have different resolutions, using

them to construct a starting  $V_P/V_S$  model will produce some unrealistic values and potentially bias inversion in the second step. Therefore, for the second set of starting models, the  $V_P$  model still comes from the first step, whereas the starting  $V_P/V_S$  model is assumed with a uniform value of 1.75. The tomographic inversion includes 9 iterations of joint inversion for velocity and relocation as well as 6 iterations of inversion for only relocation. The  $V_P$  and  $V_P/V_S$  models are always inverted

simultaneously to avoid mapping errors in one model into the other. As shown in Fig. 3, the output  $V_P/V_S$  models given two different starting models are similar. Therefore, we prefer the inverted  $V_P$  and  $V_P/V_S$  models with a starting  $V_P/V_S$  value of 1.75 (Figs. 3a, 3c, 4–6). Details of the data preparation and inversion are described in Supplementary Text S1.

Although our tomography method does not require a slab surface (i. e., the top of the plate interface), we also construct a geometry model of the slab surface for interpretation. This model is based on a model constrained by active-source seismic experiments (Kuehn, 2019) in addition to the Slab2 model (Hayes et al., 2018). We start with the Slab2 model as the slab surface geometry (Hayes et al., 2018) (Fig. S11a). In the regions with active-source imaging (Kuehn, 2019), we update the slab surface geometry in the Shumagin, Chignik, and Chirikof segments because these results are presumably more accurate than the Slab2 model. The slab surface becomes about 7 km deeper, particularly in the Chignik and Chirikof segments. We then add a 50-km-wide buffer zone to transit from the active-source-imaged region to the background Slab2 model.

#### 2.2. Geodetic modelling

We estimate the slip deficit along the subduction interface using the

TDEFNODE software package (McCaffrey, 2002) following Drooff and Freymueller (2021). This approach predicts velocities at the GNSS sites on the Peninsula block by combining the motions due to tectonic block rotation with the elastic deformation associated with the accumulation of interseismic slip deficit. Compared to the slip deficit model of Drooff and Freymueller (2021), we extended the slip deficit model further to the east to include the entire Kodiak Island and updated the slip deficit distribution in the eastern part of the model with more data.

We approximate the Aleutian megathrust as a series of planar dislocations in an elastic halfspace (Okada, 1992) and create a grid of nodes with 10 km spacing along the strike and 5 km spacing along the dip, assuming the Slab2 (Hayes et al., 2018) slab surface geometry from 10 to 75 km depth. Then we estimate the slip deficit at each grid node and interpolate it between the node grids. Using the updated slab surface model from Section 2.1 will result in negligible changes on the estimated slip deficit along the strike and small changes along the dip, because the maximum change in the slab surface depth is only  $\sim$ 7 km.

We define block boundaries, angular velocities, and rotational poles according to the published data from the Peninsula (Li et al., 2016), Southern Alaska (Fletcher and Freymueller, 2003), and the Bering (Cross and Freymueller, 2008). The Pacific and North American plate boundaries and rotational poles are defined by Argus et al. (2010). All sites in this study lie on the Peninsula block, and the relative motion of

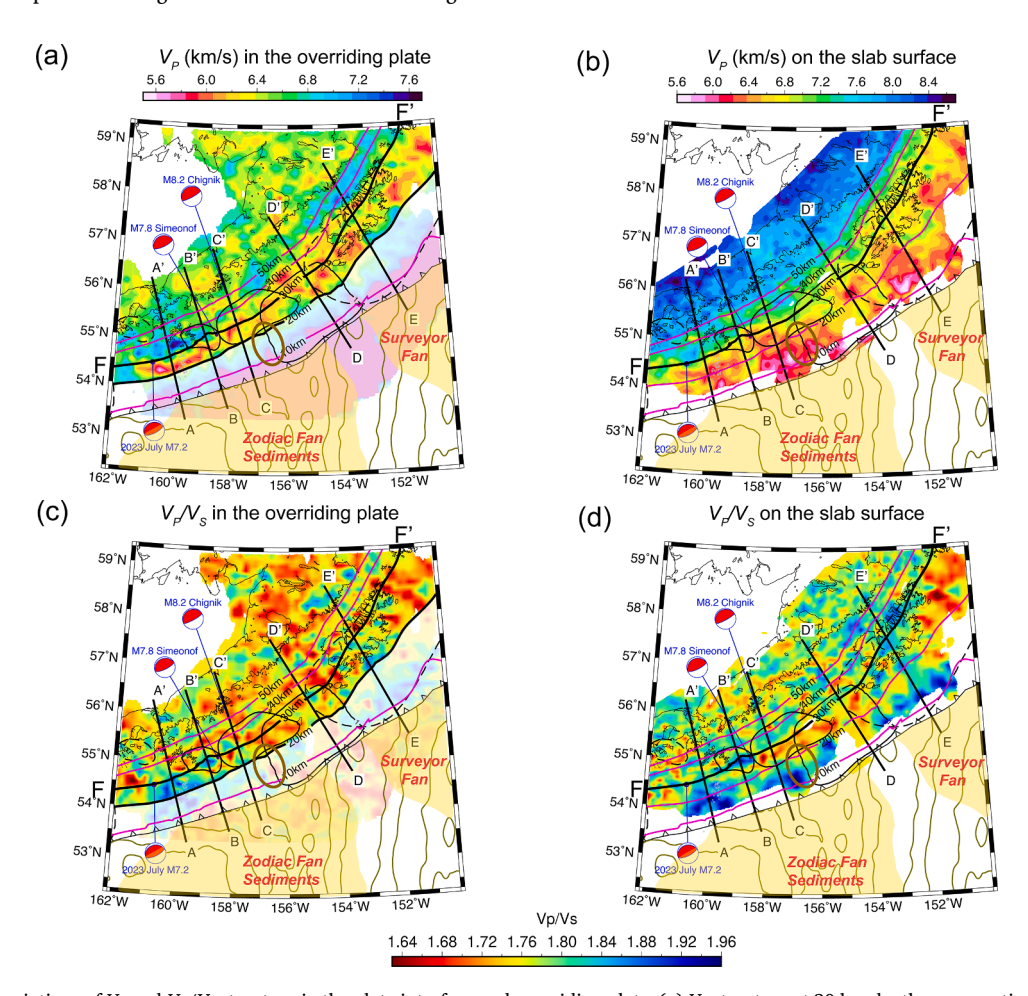
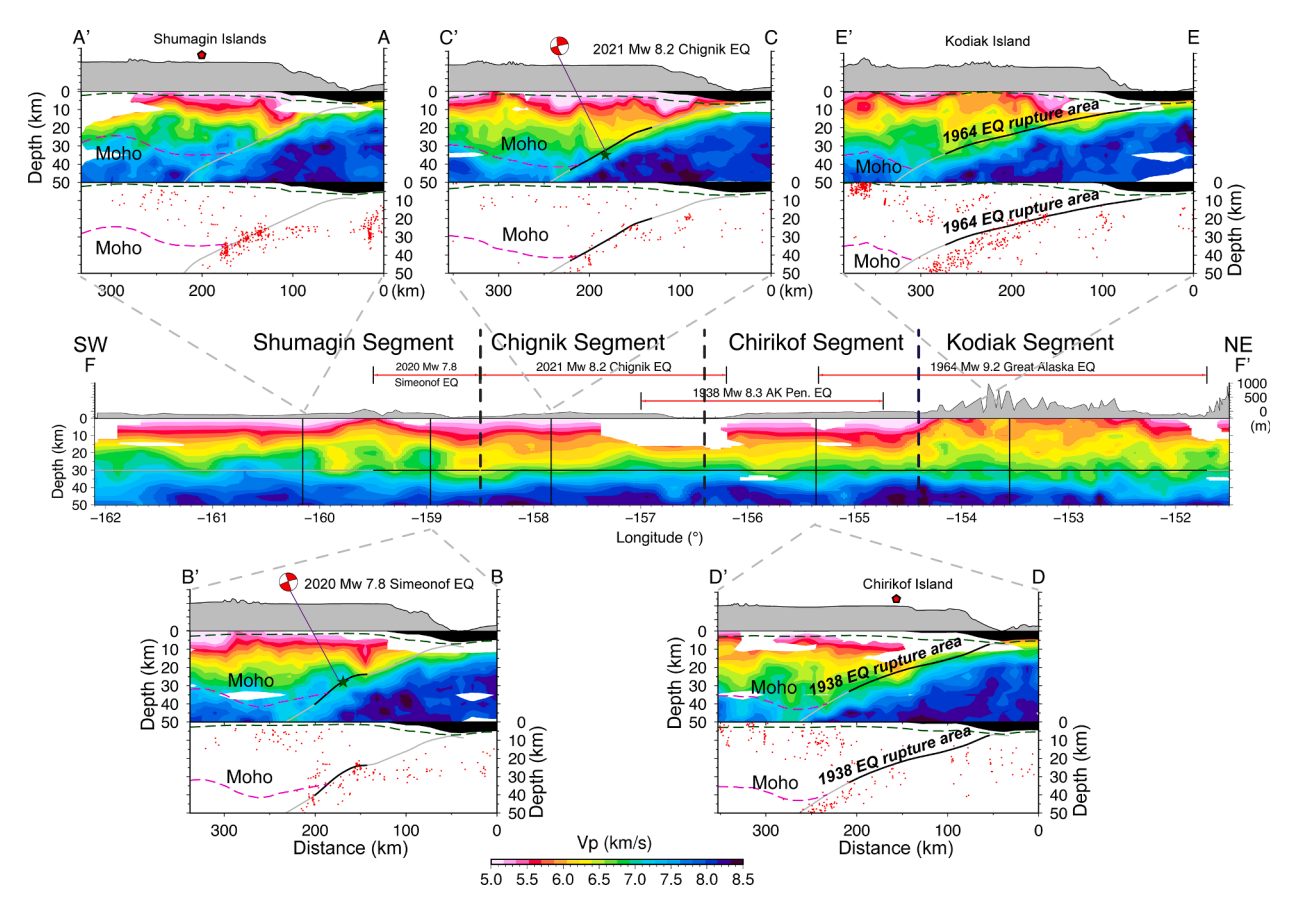


Fig. 4. Along-strike variations of  $V_P$  and  $V_P/V_S$  structure in the plate interface and overriding plate. (a)  $V_P$  structure at 20 km depth, representing the overriding plate. Regions with low resolutions are masked. The area southeast of the 20 km depth contour of the slab surface is semi-transparently masked because this area is within the subducted slab rather than the overriding plate. Dark yellow contours on the Pacific Plate outline seafloor magnetic anomalies (Meyer et al., 2017). Yellow-shaded areas show significant sediment input to the trench (von Huene et al., 2012). The thick brown contour up-dip of the 2021 M8.2 Chignik rupture zone indicates the area of a slow slip event in 2018 (He et al., 2023). Bold black lines indicate the cross-sections in Figs. 5 and 6. Other features are the same as Fig. 1. (b)  $V_P/V_S$  structure on the slab surface. The slab surface geometry is based on a model constrained by active-source seismic experiments (Kuehn, 2019) in addition to the Slab2 model (Hayes et al., 2018). Other features are the same as in (a). (c) and (d) show the  $V_P/V_S$  structure in the overriding plate and at the plate interface, respectively. Other features are the same in (a) and (b).



**Fig. 5.** *V<sub>P</sub>* structure along 6 cross-sections shown in Fig. 4. Cross-sections A-A' to E-E' are normal to the trench, whereas F-F' is along the 30-km depth contour of the slab surface and is perpendicular to all other cross-sections. In each panel, the grey curve shows the slab surface based on the Slab2 (Hayes et al., 2018) model and with the geometry changes constrained by previous active-source seismic studies (Kuehn, 2019), and the black parts indicate the rupture areas of previous megathrust earthquakes. The dark-green and red dashed curves show the bottom of the sediment layer and the overriding plate Moho, respectively, based on an independent surface-wave tomography study (Li et al., 2024). Vertical black dashed lines in F-F' show the segment boundaries. Red bars above F-F' indicate the rupture areas of previous megathrust earthquakes. Regions with low resolutions are masked. Topography/bathymetry is plotted on the top of each panel with vertical exaggeration. The relocated earthquake distribution (red dots) in each cross-section is right below the velocity model.

the Peninsula block and Bering Plate is small (Cross and Freymueller, 2008; Elliott and Freymueller, 2020; Li et al., 2016). Therefore, we assume that the Alaska-Aleutian subduction zone is the only source of substantial elastic strain accumulation. We invert for slip deficit using only the horizontal components of site velocities. The vertical site velocity residuals are ~3 mm/yr in our results. Thus, long-wavelength patterns are likely due to the inaccuracies of regional Glacial Isostatic Adjustment models for the collapse of the forebulge of the Laurentide ice sheet as well as inaccurate loading models of the historic glaciers in the Alaska Peninsula (Li and Freymueller, 2018). The velocities of the sites in the Alaska Peninsula and west of Kodiak are taken from Drooff and Freymueller (2021), including their corrections to remove the volcanic inflation signal from Veniaminof volcano. We use velocities from Elliott and Freymueller (2020) for sites in the Kodiak archipelago. They are derived from the same set of daily GNSS solutions, and simply represent different spatial subsets.

We divide up the subduction interface into discrete segments, using the same segment boundary locations as Drooff and Freymueller (2021) (5-segment model) outboard of the Shumagin and Semidi Islands. We test the effect of an additional coupling boundary inserted near Tugidak Island in the southwestern Kodiak archipelago (6-segment model), corresponding to the boundary between the Chirikof and Kodiak segments (Fig. 7). We assume a Gaussian distribution along the dip for the slip deficit in each segment. The slip deficit is uniform within each segment, but there is no enforced along-strike smoothing between segments (Li and Freymueller, 2018; Drooff and Freymueller, 2021). The

Gaussian model predicts a much lower slip deficit at shallower depths than the model that assumes the slip deficit monotonically decreases with depth (Drooff and Freymueller, 2021; Xiao et al., 2021). Compared to the monotonic model, the Gaussian model leads to a lower slip deficit near the trench, which may help explain the lack of a significant tsunami. We are unable to distinguish between the Gaussian and monotonic coupling models based on the onshore data alone, but both are useful in providing endmember scenarios for minimum and maximum extents of the coupling patches. We choose to regularize our coupling model using a Gaussian method in order to provide a minimum extent of the regions of coupling as required to fit the onshore geodetic data.

#### 3. Results

#### 3.1. Seismic tomography images

Our results reveal the seismic velocity structure shallower than 50 km depth, extending from the Alaska Trench to arc volcanoes on the Alaska Peninsula (Figs. 4–6). Compared to a recent body-wave tomography study using a similar dataset (Gou et al., 2022), our results show similar large-scale patterns but provide a much higher resolution. This is because our method is more sensitive to small-scale anomalies in the earthquake source region, and we minimize any systematic biases by simultaneously inverting for  $V_P$ ,  $V_P/V_S$ , and earthquake hypocenters. A gently dipping high- $V_P$  structure ( $\sim$ 6.6–8.5 km/s) is imaged beneath the

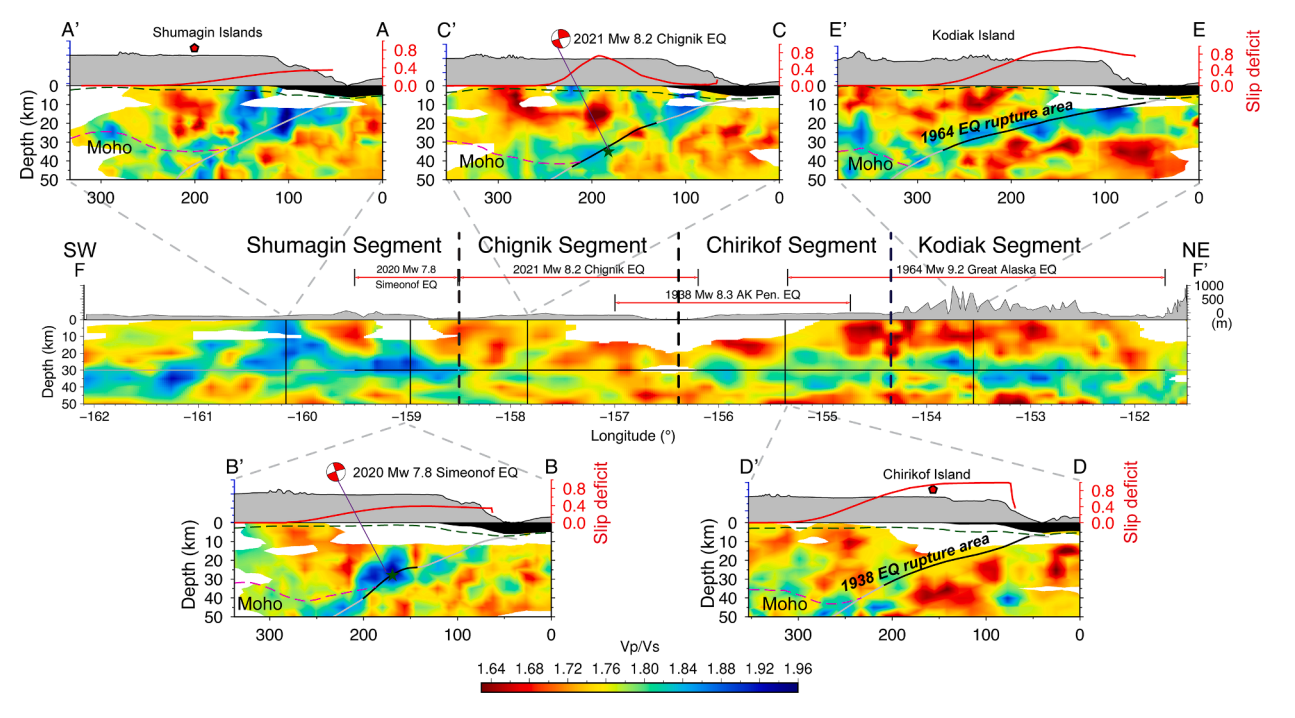


**Fig. 6.**  $V_P/V_S$  structure along 6 cross-sections shown in Fig. 4. Other features are the same as in Fig. 5 except that the relocated events are not shown here. Cross-section F-F' is in the Chugach terrane from northeast to southwest despite the along-strike changes in  $V_P/V_S$ . The slip deficit from Fig. 7 along each cross-section is shown as red curves atop the velocity structure.

slab surface (Fig. 5). The overriding plate at 20 km depth shows higher  $V_P$  values (~7.2–7.5 km/s) in the Shumigan segment compared to the segments to the east (Fig. 4a). But we do not observe dramatic changes in  $V_P$  on the slab surface (Fig. 4b).

The  $V_P/V_S$  structure shows strong variations along the strike in the overriding plate and on the slab surface (Figs. 4c, 4d, 6). We do not observe  $V_P/V_S$  anomalies higher than 2.0, such as was imaged by studies of receiver functions in the Cascadia subduction zone (Audet et al., 2009), possibly because our tomography models have relatively lower spatial resolution. In the Shumagin segment to the southwest, the overriding plate and slab surface show a high  $V_P/V_S$  signature from near the trench to ~40 km depth (Figs. 4, 6). In the Chignik and Chirikof segments to the east, low  $V_P/V_S$  anomalies are the dominant features in the overriding plate and on the slab surface at depths greater than 20 km. At depths shallower than 20 km towards the trench, the slab surface shows a high  $V_P/V_S$  in the Chignik segment but low  $V_P/V_S$  in the Chirikof segment. In the Kodiak segment further to the northeast, the overriding plate displays low  $V_P/V_S$  anomalies, but the plate interface shows high  $V_P/V_S$  values (Fig. 6). These strong along-strike changes of  $V_P/V_S$ structures in each segment are moderate-scale features with sizes larger than 40 km horizontally and 10 km vertically.

#### 3.2. Seismic tomography resolution tests

To evaluate the tomography model resolution, we perform 4 synthetic tests with different input models (details in Supplementary Text S1.2). The first and second tests are checkerboard tests with different sizes of input velocity anomalies to evaluate the spatial resolution (Figs. S1-S3). The third and fourth restoration tests are designed to validating our capability of imaging high  $V_P/V_S$  anomarlies at the plate interface with along-strike variations (Figs. S4–S7). The recovered checkerboard models suggest that the slab structure is well imaged at 20–40 km depths, particularly near earthquake sources (Fig. S1–S3). In the first checkerboard test (Fig. S1), we calculate the semblance between the recovered and input models at each node, and use it as a proxy for model resolvability (Zelt, 1998). By visually comparing the input and recovered models, we choose the semblance value of 0.54 as the

threshold of model resolvability and use this contour to mask out the low-resolution regions in the final  $V_P$  and  $V_P/V_S$  velocity models. As shown in Figs. S1-S3, we achieve a resolution of 25 and 10 km in the horizontal and vertical directions, respectively, in the unmasked region. Therefore, we focus on discussing large-scale ( $\geq$ 30 km horizontally and  $\geq$ 10 km vertically) structures in our models because some small-scale (<20 km horizontally) anomalies may reflect model resolution changes along the strike and dip directions due to ununiform distributed stations and earthquakes.

The third resolution test shows that the high  $V_P/V_S$  layer at the plate interface, representing hypothetically hydrated slab sediment and crust, can be well recovered at 15–50 km depths throughout the region (Fig. S4). In addition, the high  $V_P/V_S$  anomaly in the overriding plate, representing a possible fore-arc sedimentary basin, will not be mistakenly mapped to greater depths. Therefore, we are confident with the imaging results near the plate interface. In addition, the similar patterns between the input and recovered models in the fourth resolution test indicate the major along-strike changes are robust in our tomography images (Figs. S5-S7).

In summary, all resolution tests suggest that our  $V_P/V_S$  model has a horizontal resolution of 25 km in the unmasked regions. Thus, we are confident with all moderate-scale anomalies that are mentioned in Section 3.1 and will be discussed in Section 4. Our resolution limit is larger than the typical width of the plate interface deformation zone (<10 km) or the scale of fluid-rich layers (<1 km) (Li et al., 2015). Therefore, the  $V_P$  and  $V_P/V_S$  structures imaged at the slab surface represent the average velocity structure across the plate interface.

#### 3.3. Plate coupling model

We find a  $\sim$ 14 % decrease in the total weighted residual sum of square velocities for sites fit in the 6-segment model than in the 5-segment model which does not include the new boundary near Tugidak Island, and assumes the Chirikof and Kodiak segments have the same slip deficit distribution. The best-fit coupling distributions and residual site velocities are shown in Fig. 7. The main new feature of this model is the higher slip deficit outboard of Kodiak than in the Chignik

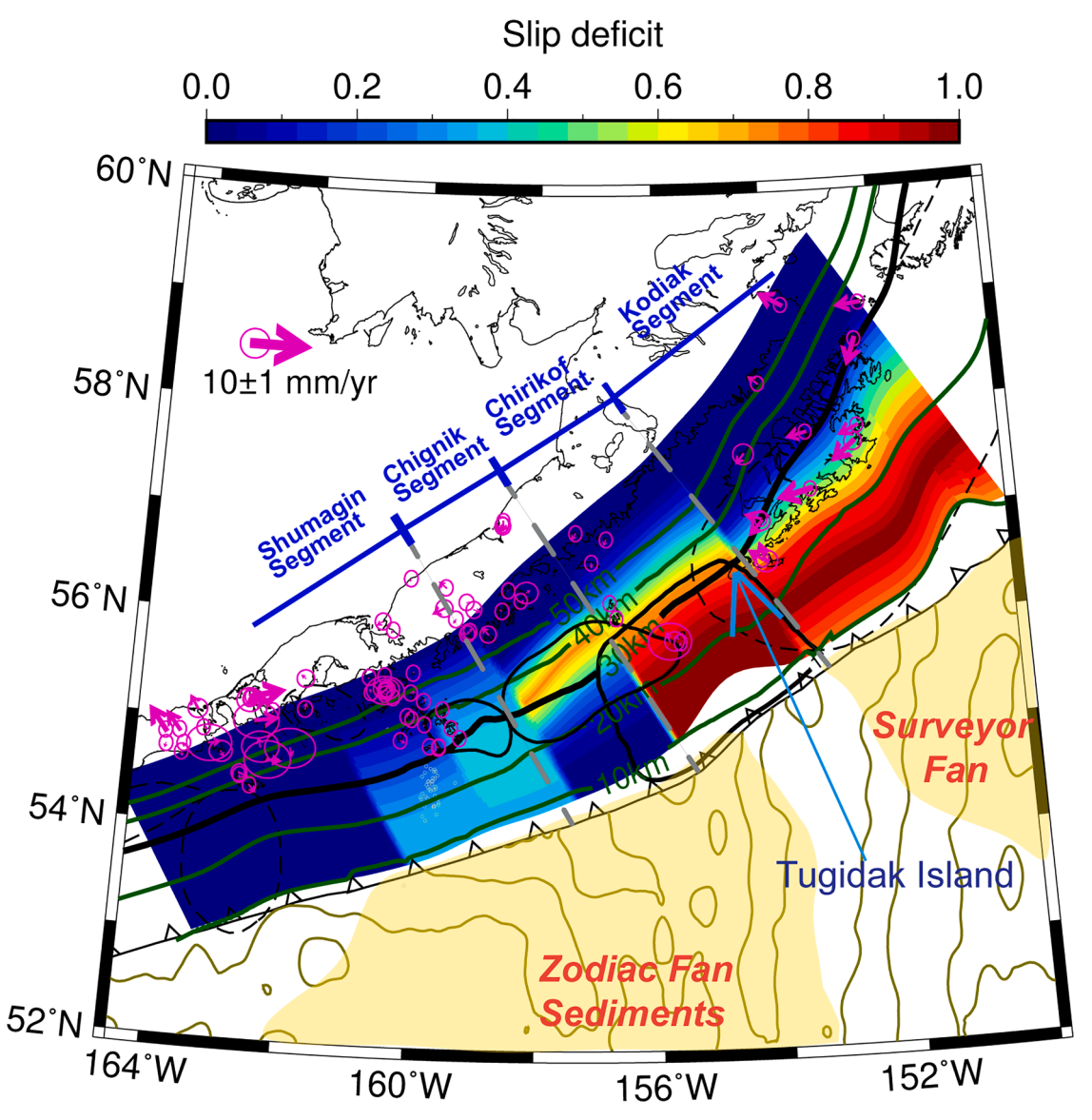


Fig. 7. New slip deficit model constrained by geodetic data from 1992 to 2017. Compared to the previous model by Drooff and Freymueller (2021), we add an additional segment boundary near Tugidak Island (pointed by the light blue arrow) between the Kodiak and Chirikof segments. The magenta ellipses and vectors indicate the data uncertainties and the misfit of GNSS stations using the new slip deficit model, respectively.

segment and the high slip deficit outboard of Chirikof Island. In addition, the new slip deficit model has a narrower highly locked patch in the Kodiak segment than the previous model (Drooff and Freymueller, 2021), and this highly locked patch is at a shallower depth compared with the one in the Chignik segment. The nearly 100 % slip deficit outboard of Kodiak is similar to that found in models that were optimized for the 1964 rupture zone (i.e., Elliott and Freymueller, 2020; Suito and Freymueller, 2009). We note that our model includes a zone of partial coupling by the trench outboard of Kodiak where the model resolution is minimal. The estimated slip deficit at shallow depth is controlled mainly by the model regularization rather than the data.

We observe a distinct trend of trench-parallel residual velocities for sites on Kodiak Island (Fig. 7), which we interpret as unaccounted-for localized forearc translation on the order of  $\sim 5$  mm/yr at most sites. This is a common phenomenon observed in subduction settings globally (Jarrard, 1986; Wang et al., 2003). In the case of Kodiak, this effect was accounted for in Elliott and Freymueller (2020) by adding an upper crustal strike-slip fault aligned approximately with the 25 km depth contour underneath Kodiak Island which bounded two upper plate blocks. We note that the transition from partial coupling to creeping

beneath Kodiak in our model is in the same place as the along-strike upper crustal fault included by Elliott and Freymueller (2020). However, it will dramatically increase the model misfit in the Chirikof segment if we add a creeping boundary west of the Kodiak segment in the same location as in Elliott and Freymueller (2020). In order to test whether this crustal sliver affects the estimated slip deficit distribution. we projected the Kodiak site velocities into the trench-normal direction and re-ran the inversion for slip deficit without the trench-parallel motion. We find no difference in the coupling model from such a model run. Therefore we conclude that the effect of a Kodiak crustal sliver on the coupling model is negligible and the misfit caused by the projection will be passed on into the residuals rather than biasing the model parameters. Besides, adding an additional block to the model would require us to adopt the estimated block velocity from Elliott and Freymueller (2020). This additional block velocity was not purely trench parallel and it is provided to achieve a better fit to the GNSS data further to the east, which is outside of our study area. Geodetic modeling of this additional block will require to extend the model domain even further east by adding more data to help constrain the block motion, and re-considering block boundaries in a complex region outside of our study area.

#### 4. Discussions

# 4.1. Geological implications of $V_P/V_S$ anomalies and effects of seismic anisotropy and slab geometry

In this study, we focus on the  $V_P/V_S$  images while also using the  $V_P$ model to help with interpretation. We estimate the  $V_P$  and  $V_P/V_S$  of potential compositions on the Alaska slab surface using a MATLAB toolbox developed by Abers and Hacker (2016), and compare them with the  $V_P$  and  $V_P/V_S$  values in our tomography models (details in Supplementary Text S2.1; Fig. S8). The comparisons suggest that the extremely high  $V_P/V_S$  (>1.83) anomalies on the slab surface indicate the existence of fluids. In addition, we evaluate the effects of the azimuthal anisotropy, titled transversely isotropy, and sub-slab anisotropy in the asthenosphere on the along-strike variations of the  $V_P/V_S$  anomalies, and conclude that these effects are minor and will not change our interpretations (details in Supplementary Text S2.2; Fig. S10). It is important to emphasize that our tomography images do not have sufficient resolution to capture details of fluid-rich layers at the plate interface that are on a scale of hundreds of meters to a few kilometers (Li et al., 2015). The  $V_P/V_S$  values of particular features are likely underestimated due to smoothing in the tomographic inversions. Therefore, we do not quantitatively translate the imaged  $V_P/V_S$  values to rock porosity. Instead, we qualitatively interpret high  $V_P/V_S$  anomalies as a proxy for fluids and hydrous minerals in highly deformed rocks and

Besides the geometry model of the slab surface described in Section 2.1, we also try other slab geometry models, including the original Slab2 model and a model purely constrained by our relocated seismicity distribution (Fig. S11a, S11b), for interpretation. In addition, we average  $V_P/V_S$  from 10 km above to 10 km below the slab surface of the chosen geometry model (Fig. S11c–e). We find no obvious changes in the alongstrike  $V_P/V_S$  variations among all the slab surface models (Fig. S11). Therefore, we conclude that the choice of the slab surface geometry has minor effects on our interpretations, partly because our tomography resolution ( $\sim$ 10 km vertically) is larger than the slab surface model discrepancies.

#### 4.2. Seismic imaging of fluids in highly deformed rocks

The subducted slab is imaged as a gently dipping ( $<30^\circ$ ) region of high- $V_P$  anomalies ( $\sim$ 6.6–8.5 km/s) beneath the slab surface (Fig. 5). A thin (<10 km) relatively lower  $V_P$  layer ( $\sim$ 6.6–6.9 km/s) overlays the high- $V_P$  anomalies ( $\sim$ 7.0–8.5 km/s) right beneath the slab surface. These layers indicate the slab crust and mantle, respectively. The slab  $V_P$  structure is in good agreement with previous active-source and receiverfunction seismic imaging in this region (Li et al., 2018a; Onyango et al., 2022; Shillington et al., 2022, 2015) (Fig. S9). The  $V_P/V_S$  structure shows more complexities, with values ranging from 1.65 to 1.90 (Figs. 4, 6). This is because  $V_P$  is dominantly controlled by bulk composition, temperature, and pressure, whereas  $V_P/V_S$  is highly sensitive to the existence of fluids (Takei, 2002).

 $V_P/V_S$  varies with depth on the slab surface, indicating the presence of hydrous minerals and fluids from different sources (Fig. 4d). Near the trench at 10–20 km depths, we observe high  $V_P/V_S$  anomalies in almost all segments, in agreement with the fluid overpressure observed in other subduction zones from rock experiments and seismic studies (Bassett et al., 2014; Tobin and Saffer, 2009). Furthermore, a recent study using absolute pressure gauge data from the AACSE detected a possible slow-slip event in late 2018 near the trench (He et al., 2023), also implying high fluid content at shallow depths. At greater depths, the distribution of high  $V_P/V_S$  anomaly varies.

The fluids at depths shallower than 20 km presumably come from sediment compaction, whereas the sources for fluids at 20–50 km depths remain under debate. Some numerical simulations suggest that the Alaska slab is cold at these depths and that slab dehydration primarily

happens below 70 km (Abers et al., 2017), although a recent study demonstrated that the metamorphic dehydration reactions may take place at shallower depths if non-steady-state thermal evolution of the slab is considered (Holt and Condit, 2021). A recent electromagnetic study in the Shumagin segment suggests that slab mantle dehydration may provide substantial fluids in the fore-arc (Cordell et al., 2023). Nevertheless, we attribute the high  $V_P/V_S$  anomalies in the subducted slab to the locally hydrated slab crust and fluids either from *in-situ* dehydration or from migration along the plate interface up-dip from deeper sources. The high  $V_P/V_S$  anomalies imaged in the overriding plate crust indicate fluids migrating from the plate interface because we do not expect any dehydration reactions in the fore-arc crust.

We observe systematic along-strike variations in  $V_P/V_S$  and thus the inferred fluid content (Fig. 6). We acknowledge that the model resolution changes along strike as the station and earthquake distributions are not uniform. However, we focus on velocity anomalies on a scale of >30 km horizontally and >10 km vertically, which are well resolved across the entire study region (Figs. S1-S7). These anomalies are likely smoothed images of geological features, such as the interplate deformation zone or localized fluid-rich pockets, which are on a scale smaller than our tomography resolution. Thus, the imaged velocity values should not be over-interpreted. The Shumagin segment (represented by cross-sections A-A' and B-B' in Fig. 6) is characterized by continuous high  $V_P/V_S$  anomalies (1.86–1.90) and high fluid content both at the plate interface and in the overriding plate crust. Interestingly, the fluid distribution inferred from a recent 2D electromagnetic study (Cordell et al., 2023) is nearly identical to that inferred from our cross-section B-B', showing a fluid-rich plate interface at ~30 km depth and a fluid-starved plate interface shallower than 25 km. However, this electromagnetic profile is located near our cross-section A-A', where we image a fluid-rich plate interface from 30 km to at least 10 km depth. We suspect the discrepancies between the 2D electromagnetic profile with our 3D seismic images result from the along-strike variations within the Shumagin segment that cannot be captured by a 2D profile. Our 3D images show that the megathrust at shallow (<25 km) depths is more hydrated than that revealed by Cordell et al. (2023), although the fluid distribution is not uniform throughout the entire Shumagin segment.

In contrast to the Shumagin segment, moderately high  $V_P/V_S$ anomalies (1.80–1.84) are sporadically observed at the plate interface in the Chignik and Chirikof segments (represented by cross-sections C-C' and D-D' in Fig. 6, respectively), whereas low  $V_P/V_S$  anomalies dominate the overriding plate there, implying dry conditions in these segments. In the Kodiak segment (represented by cross-section E-E' in Fig. 6), the plate interface has high  $V_P/V_S$  anomalies (1.82–1.86), indicating high fluid content, whereas the overriding plate shows low  $V_P/V_S$  and low inferred porosity. Cross-section F-F' in Fig. 6 shows the  $V_P/V_S$  structure along the 30-km depth contour of the slab surface, suggesting that the plate interface and overriding plate crust are more hydrated in the Shumagin segment than the segments to the east. This trend is in good agreement with active-source seismic studies which suggest more water subducted in the southwest than in the northeast (Shillington et al., 2015). The changes along cross-section F-F' can also explain the along-strike variations in azimuthal anisotropy revealed by teleseismic shear-wave splitting (Lynner, 2021), as the highly hydrated slab at 20-40 km depths in the Shumagin and Kodiak segments produce trench-parallel-fast-direction signals.

#### 4.3. Fluids enhance interseismic slip along the megathrust

The  $V_P/V_S$  images at the slab surface and in the overriding plate show first-order similarities with our updated slip deficit model, with  $V_P/V_S$  anti-correlating with slip deficit along the dip (Fig. 6) and along the strike (Fig. 8), except in the near-trench area where the seismic and geodetic model resolutions are both limited. In the Shumagin segment to the southwest, high  $V_P/V_S$  anomalies at the plate interface and in the overring plate coincide with low slip deficit and high seismic activity,

# Variations of $V_P/V_S$ , seismic activity, and slip deficit along strike

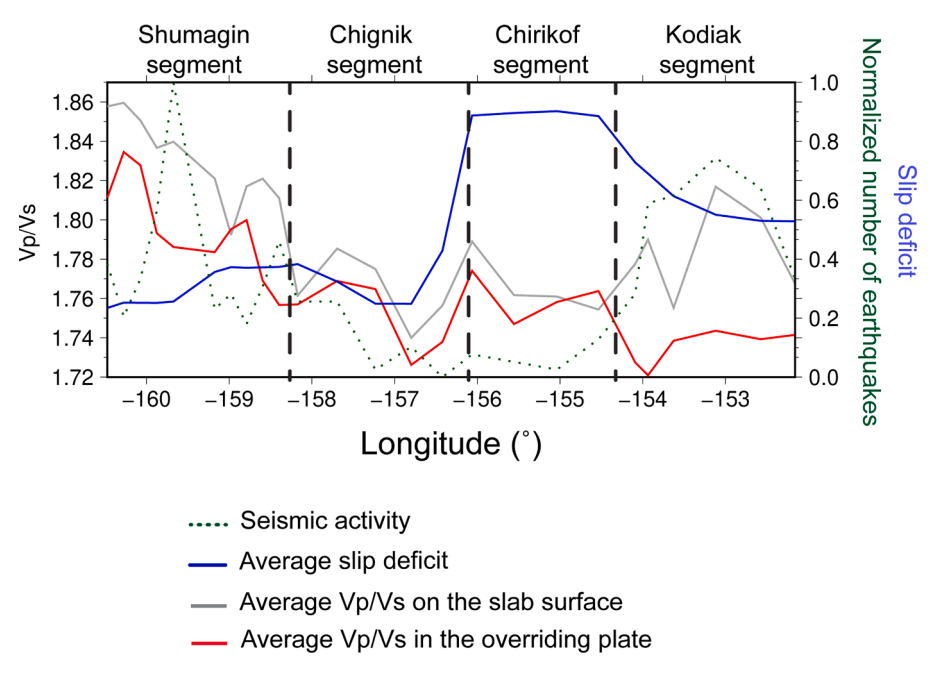


Fig. 8. The comparison of the new slip deficit model with the  $V_P/V_S$  structure along the strike. The red, grey, blue, and dotted green curves indicate the average  $V_P/V_S$  on the slab surface, average  $V_P/V_S$  in the overriding plate, average slip deficit, and seismic activity, respectively. All the average values are derived by taking the average of the structure between 15 and 35 km depths along the slab surface or in the overriding plate. The number of earthquakes within a 30-km-wide along-dip cross-section is normalized by the largest number of earthquakes along the strike.

suggesting abundant fluids enhance interseismic creep along the megathrust (Figs. 4, 6, 7). In contrast, in the Chignik segment to the northeast, low  $V_P/V_S$  anomalies at the plate interface and in the overriding plate, a higher slip deficit, and low seismic activity imply that the low fluid content inhibits interseismic creep and promotes frictional locking. Further to the northeast, the Chirikof segment, which has the widest region of high slip deficit has moderate-to-low  $V_P/V_S$ , implying a dry plate interface. At the north-eastern end of this region, the Kodiak segment has a high slip deficit and high  $V_P/V_S$  anomalies at the plate interface but low  $V_P/V_S$  in the overriding plate. In Fig. S13, we also compare our  $V_P/V_S$  model with the slip deficit model from Zhao et al. (2022a), which models interseismic plate coupling with asperities based on historical and recent rupture zones. This comparison shows a similar anti-correlation between  $V_P/V_S$  and interseismic slip deficit.

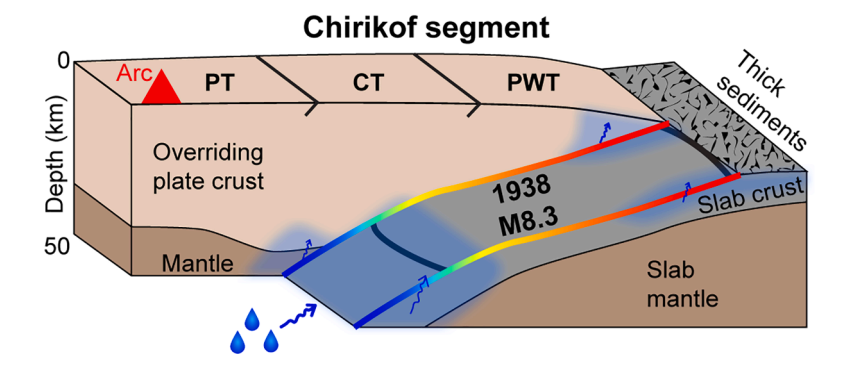
The contrast in the Kodiak segment is surprising, given that many studies suggest that fluids at the plate interface should enhance the interseismic slip along the megathrust (Audet et al., 2009; Guo et al., 2021; Heise et al., 2017; Kodaira et al., 2004; Li et al., 2018a; Moreno et al., 2014). But our observation is not the only case that shows an anti-correlation between  $V_P/V_S$  in the overriding plate and slip deficit. For example, a recent tomography study of the Honshu subduction zone (Zhao et al., 2022b) using offshore seismic data shows that  $V_P/V_S$ changes little at the megathrust, but reduces dramatically in the overriding plate from northern Honshu to central Honshu, coinciding with the increase in interseismic slip deficit and the 2011 M9.1 Tohoku-Oki earthquake rupture area. In the Hikurangi subduction zone, Henrys et al. (2020) also image an increase in  $V_P/V_S$  in the forearc overriding plate from the southern North Island to Cook Strait, anti-correlating with the slip deficit change. In the southern Cascadia subduction zone with a high slip deficit, high  $V_P/V_S$  anomalies are confined within the slab crust and low  $V_P/V_S$  anomalies lie above the plate interface (Delph et al., 2018; Guo et al., 2021).

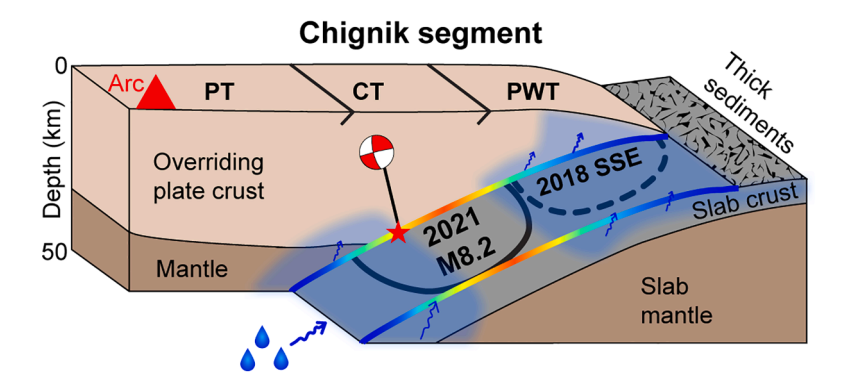
Given all observations above, we propose that the along-strike variations in interseismic megathrust slip behaviors at 20–50 km depths are

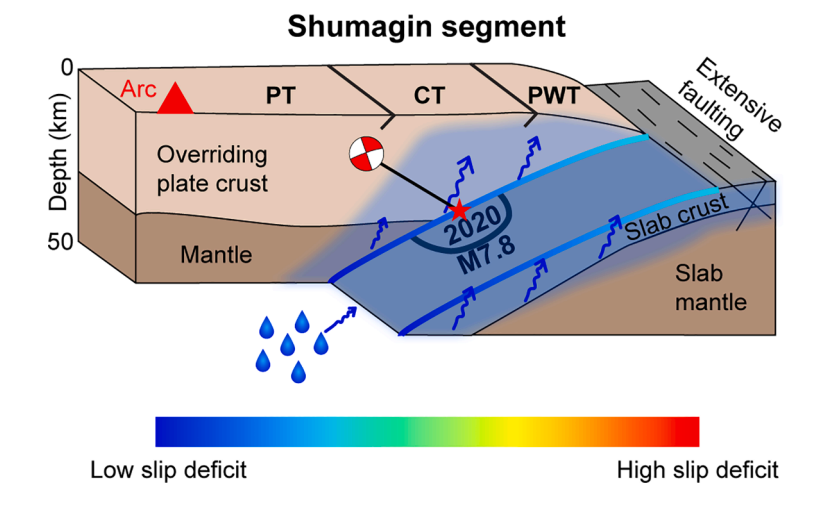
dominantly controlled by the changes in fluid content in the subduction zone, particularly in the overriding plate crust that directly contacts the plate interface at 15–35 km depths (Fig. 9). We cannot rule out the other factors, such as the plate interface roughness and changes in the slab surface geometry, that may also influence interseismic slip deficit (Cordell et al., 2023; Jiang et al., 2022). However, the fluid content in the overriding plate is the most evident factor that varies along the strike and well anti-correlates with the interseismic slip deficit.

Systematic changes in the hydration state of the plate interface are presumably caused by the varying input of the incoming plate and the slab dehydration after subduction. The hydration state of the overriding plate is fundamentally affected by the permeability of the overriding materials and the fluid supply from the plate interface. It is worth noting that some previous studies suggest that changes in the overriding plate lithology, such as the deposit of quartz into the overriding forearc crust, can affect the inter-plate slip behaviors (Audet and Burgmann, 2014). Here at the Alaska Peninsula, two major Mesozoic and Paleogene tectonic boundaries cut across all the boundaries between segments with different slip deficits (Horowitz et al., 1989). The Border Ranges fault system (BRFS) formed when the Chugach terrane was juxtaposed against and beneath the Peninsula terrane to the north starting from the early Jurassic (Plafker et al., 1994), and the Prince William terrane was underthrust by the Chugach terrane along the Contact fault system (CFS) further south (Fig. S12). Since both the BRFS and CFS are parallel to the trench, we do not expect significant changes in the overriding plate lithology along the strike (cross-section F-F' is in the same Chugach terrane from Fig. S12). Therefore, we suspect that the along-strike variations in  $V_P/V_S$  are predominantly influenced by the fluid supply from slab dehydration rather than the overriding plate lithology. We propose that the flux of fluids across the plate interface has a greater influence on the slip behavior than simply the presence of fluids along the interface. The high fluid pore pressure that decreases the effective normal stress is important but not the most critical factor in controlling the megathrust interseismic slip deficit at the Alaska Peninsula. A high fluid flux from

# Kodiak segment Overriding plate crust Mantle Slab mantle







(caption on next page)

Fig. 9. Schematic cartoons showing fluids at the plate interface and in the overriding plate enhancing interseismic slip on the megathrust. Semi-transparent blue shades mark the fluid-rich regions revealed by high  $V_P/V_S$  anomalies. Wavy arrows indicate fluid migration, and water drops represent the possible fluid migration from deep sources. Black contours outline the rupture areas of previous megathrust earthquakes shown in Fig. 1, whereas the beachballs and stars represent the hypocenters of the 2020 M7.8 Simeonof and 2021 M8.2 Chignik earthquakes. The dashed black contour up-dip of the 2021 M8.2 Chignik earthquake rupture zone shows the area of the 2018 slow slip event in the Chignik segment. The color-coded curves on each plate interface illustrate the slip deficit in each segment. Black lines on the surface represent the terrane boundaries between the Prince William terrane (PWT), Chugach terrane (CT), and Peninsula terrane (PT). Note that the inferred properties of the overriding plate crust do not correlate with geological terranes, suggesting that the overriding plate lithology is not the predominant factor in controlling the observed along-strike variations.

the subducting plate through the plate interface would lead to the formation of clay minerals that promote fault creep, through processes of alteration, dissolution, and re-precipitation of mineral grains (Ikari et al., 2009; Katayama et al., 2015).

In the Shumagin segment, the incoming plate crust and uppermost mantle are highly hydrated through extensive outer-rise bending faults (Li et al., 2024; Liu et al., 2022b; Shillington et al., 2015) (Fig. 9). As this hydrated plate subducts, hydrous minerals in the slab crust and mantle releasing water, and triggering intermediate-depth earthquakes (Cordell et al., 2023; Wei et al., 2021). The released fluids migrate up-dip along the strongly deformed plate interface (Kuehn, 2019; Shillington et al., 2022), and hydrate the overriding plate. In addition, a thin, heavily faulted sediment layer subducts in this segment (Li et al., 2018a). Consequently, the combination of more fluids and high deformation at the plate interface, high porosity in the overriding plate, and the lack of sediment facilitate interseismic megathrust slip, resulting in more small earthquakes but a lack of great earthquakes. In contrast, the incoming plate is less faulted and hydrated with more sediments subducted in the Chignik segment (Li et al., 2018a; Li et al., 2024; Shillington et al., 2015), and thus less water is subducted to great depths to trigger intermediate-depth earthquakes (Wei et al., 2021). The low fluid supply from deep dehydration, combined with the weakly deformed plate interface, a thick sediment layer, and a low-porosity overriding plate, result in a lower aseismic fault slip, and thus fewer small earthquakes but several great events in the past. In the Chirikof segment further to the east, the plate interface from the trench to ~30 km depth and the overriding plate crust are so dry that the two plates are fully frictionally locked. In the Kodiak segment at the eastern end, the incoming plate is more hydrated compared to that in the Chirikof segment, because more normal faults that are sub-parallel to the trench are re-activated at the outer rise (Reece et al., 2013) and several seamounts enter into the trench (von Huene et al., 2021). Consequently, more water is subducted to great depths and then released to form a sporadically fluid-rich plate interface, which is consistent with petrological studies of exhumed fore-arc rock (Vrolijk, 1987) and a slow-slip event in 2009 at 20-40 km depths (Holtkamp, 2017). However, the overriding plate crust remains relatively dry, possibly because the less deformed lower crust of Kodiak Island acts as a permeability barrier above the plate interface (Saffer and Tobin, 2011), resulting in a lack of fluid flux across the interface and through the rocks along the interface. Therefore, the interseismic megathrust slip deficit is high in this region.

#### 4.4. Complicated roles of fluids in generating megathrust earthquakes

Our seismic images and interseismic slip deficit model help explain the diverse mechanisms of historical and recent megathrust earthquakes at the Alaska Peninsula (Davies et al., 1981; Elliott et al., 2022). Note that the velocity anomalies and the inferred high-porosity regions are possibly more concentrated than those appearing in our tomography images. The 2020 M7.8 Simeonof earthquake ruptured down-dip from 25 to 40 km depths and propagated westward within the Shumagin segment (Xiao et al., 2021; Ye et al., 2021) (Figs. 4d, 6). This segment is characterized by a low interseismic slip deficit ( $\sim$ 25 % of the plate motion rate), extremely high  $V_P/V_S$  anomalies and thus high fluid content at the plate interface and overriding plate, and a lack of great megathrust earthquakes (M > 8) for at least 200 years. However, the

Simeonof earthquake rupture initiated near the boundary between the Shumagin and Chignik segments where  $V_P/V_S$  changes from high to low and the slip deficit changes from low to moderate (Figs. 4d, 7). We suspect that shear stress had accumulated due to the stress shadow effect of the adjacent Chignik segment, and high fluid content lowered the plate interface strength to facilitate rupturing. Northeast of the Shumagin segment, the 2021 M8.2 Chignik earthquake nucleated in a high  $V_P/V_S$  region and ruptured into low  $V_P/V_S$  regions in both the down-dip and eastward directions (Figs. 4d, 6). The rupture area occurred from 20 to 40 km depths within the moderately high slip deficit region of the Chignik segment (Elliott et al., 2022; Liu et al., 2022a). We propose that this earthquake started in a fluid-rich region and mainly ruptured the dry plate interface. So the relatively dry, partially locked Chignik segment acted as a barrier for the 2020 Simeonof earthquake rupturing, and then was ruptured by the 2021 Chignik earthquake. These diverse slip behaviors of fault barriers have been seen in numerical simulations (Molina-Ormazabal et al., 2023).

Although the rupture area of the 1938 M8.3 Alaska Peninsula earthquake remains under debate, it likely ruptured from near the trench to 30 km depth and overlaps with the eastern part of the 2021 Chignik earthquake rupture area (Freymueller et al., 2021). More than 80 years after this earthquake, our results show low fluid content and high slip deficit in this region. The southwestern end of the 1964 M9.2 Great Alaska earthquake exhibits a high slip deficit and low  $V_P/V_S$  in the overriding plate crust. The low  $V_P/V_S$  anomalies reflect either a low-permeability overriding plate or a low fluid supply from slab dehydration in this region, and nevertheless indicate stronger materials above the plate interface. We speculate that it is the low-porosity overriding plate rather than the fluid-rich plate interface that increases interseismic slip deficit, as the high rigidity and density of the overriding plate favor the accumulation of elastic strain at the plate interface (Sallares and Ranero, 2019; Sun et al., 2020). More sophisticated laboratory and numerical experiments focusing on the overriding plate rigidity are needed to verify our speculation. Similar conditions have been observed beneath the southern North Island, New Zealand (Henrys et al., 2020) and southern Cascadia (Guo et al., 2021). The low-porosity overriding plate may result from limited fluid flux across the plate interface because the slab dehydration appears to be weaker in the Kodiak segment compared to the Shumagin segment (Wei et al., 2021).

#### 5. Conclusions

We image the 3D high-resolution  $V_P$  and  $V_P/V_S$  structure of the megathrust and the fore-arc overriding plate at the Alaska Peninsula. We also construct a new slip deficit model at seismogenic depths and find anti-correlation between  $V_P/V_S$  and slip deficit along the strike. Fluids indicated by high  $V_P/V_S$  anomalies play an important role in controlling the along-strike variations in interseismic megathrust slip behavior at the Alaska Peninsula. In the Shumagin segment to the west, abundant fluids at the plate interface and in the overriding plate lead to a low slip deficit, less frequent large megathrust earthquakes, and higher background seismic activity. In the Chignik, Chirikof, and Kodiak segment to the east, low fluid content in the overriding plate contributes to a higher slip deficit and more frequent occurrence of great megathrust earthquakes regardless of whether the plate interface is rich or starved in fluids. Since the overriding plate shows little along-strike changes in

lithology, there is no evidence of permeability variations due to lithological changes. Therefore, we suspect that the inferred porosity variations reflect the changes in the fluid supply from slab dehydration, and a sustained fluid flux across the plate interface is critical to enhancing interseismic slip. In light of this study, we suggest future geophysical and geological observations need to pay more attention to the fore-arc overriding plate, and numerical simulations of megathrust slip need to consider the complex along-strike heterogeneities of fluid content in the overriding plate.

#### Data and code availability

Arrival time data of regional Alaska earthquakes recorded by global stations are archived at the International Seismological Center EHB bulletin (http://www.isc.ac.uk/isc-ehb/). Arrival time data for regional stations are available from the Advanced National Seismic System's Comprehensive Earthquake Catalog (http://earthquake.usgs.gov/data/ comcat/). Raw seismic data from regional stations are available at the Data Management Center of EarthScope Consortium (https://ds.iris. edu/ds/nodes/dmc/) under network IDs AK (10.7914/SN/AK). AT (10.7914/SN/AT), AV (10.7914/SN/AV), CN (10.7914/SN/CN), GM (10.7914/SN/GM), II (10.7914/SN/II), NP (10.7914/SN/NP), TA (10.7914/SN/TA), and XO (10.7914/SN/XO\_2018). GNSS velocities and station DOIs are available in the supplemental information of Drooff and Freymueller (2021) and Elliott and Freymueller (2020). Unprocessed GNSS data are available through the EarthScope Consortium (https://www.unavco.org/data/gps-gnss/data-access-methods/dai1/dai1.html). The seismic tomography models will be archived at the EarthScope/IRIS Earth Model Collaboration repository (https://ds.iris. edu/ds/products/emc-earthmodels/). The seismic tomography software packages tomoDD and teletomoDD are available upon request. The geodetic modelling software package TDEFNODE is available at https://robmccaffrey.github.io/TDEFNODE/TDEFNODE.html.

#### CRediT authorship contribution statement

Fan Wang: Methodology, Software, Validation, Formal analysis, Writing – original draft, Writing – review & editing, Visualization. S. Shawn Wei: Conceptualization, Resources, Writing – review & editing, Supervision, Project administration, Funding acquisition. Connor Drooff: Methodology, Software, Formal analysis, Writing – original draft, Visualization. Julie L. Elliott: Methodology, Software, Writing – review & editing, Visualization. Jeffrey T. Freymueller: Data curation, Writing – review & editing. Natalia A. Ruppert: Data curation. Haijiang Zhang: Methodology, Software, Writing – review & editing.

#### Declaration of competing interest

The authors declare that they have no known competing financial interests or personal relationships that could have appeared to influence the work reported in this paper.

#### Data availability

Data will be made available on request.

#### Acknowledgments

We thank D. A. Wiens and Z. Li for providing their *S*-wave velocity model of the Alaska Peninsula as our starting model prior to publication. We appreciate discussions with D. A. Wiens, D. J. Shillington, A. Gabriel, A. Bécel, H. Guo, Z. Xiao, and Z. Zhuo. We thank the AACSE PI team, particularly G. Abers, and all scientists who participated in the fieldwork for collecting the seismic data. We also thank the reviewer Roland Bürgmann for helpful comments and Hans Thybo for his editorial

handling The Generic Mapping Tools open-access software was used to produce the figures in this paper. Seismic data analysis was supported in part through computational resources and services at the Institute for Cyber-Enabled Research at Michigan State University. This work was supported by National Science Foundation grants (EAR-2052558) to J.T. F., S.S.W., and J.L.E., National Key R&D Program of China (2022YFF0800701) and the Fundamental Research Funds for the Central Universities (WK2080000144) to H.Z. F.W. and S.S.W. were also supported by the MSU Geological Sciences Endowment and Discretionary Funding Initiative.

#### Supplementary materials

Supplementary material associated with this article can be found, in the online version, at doi:10.1016/j.epsl.2024.118655.

#### References

- Abers, G.A., van Keken, P.E., Hacker, B.R., 2017. The cold and relatively dry nature of mantle forearcs in subduction zones. Nat. Geosci. 10 (5), 333–337. https://doi.org/ 10.1038/ngeo2922.
- Argus, D.F., Gordon, R.G., Heflin, M.B., Ma, C., Eanes, R.J., Willis, P., Peltier, W.R., Owen, S.E., 2010. The angular velocities of the plates and the velocity of Earth's centre from space geodesy. Geophys. J. Int. 180 (3), 913–960. https://doi.org/ 10.1111/j.1365-246X.2009.04463.x.
- Arnulf, A.F., Bassett, D., Harding, A.J., Kodaira, S., Nakanishi, A., Moore, G., 2022. Upper-plate controls on subduction zone geometry, hydration and earthquake behaviour. Nat. Geosci. 15 (2), 143–148. https://doi.org/10.1038/s41561-021-00879-x.
- Audet, P., Bostock, M.G., Christensen, N.I., Peacock, S.M., 2009. Seismic evidence for overpressured subducted oceanic crust and megathrust fault sealing. Nature 457 (7225), 76–78. https://doi.org/10.1038/nature07650.
- Audet, P., Burgmann, R., 2014. Possible control of subduction zone slow-earthquake periodicity by silica enrichment. Nature 510 (7505), 389–392. https://doi.org/ 10.1038/nature13391.
- Bassett, D., Sandwell, D.T., Fialko, Y., Watts, A.B., 2016. Upper-plate controls on coseismic slip in the 2011 magnitude 9.0 Tohoku-oki earthquake. Nature 531 (7592), 92–96. https://doi.org/10.1038/nature16945.
- Bassett, D., Sutherland, R., Henrys, S., 2014. Slow wavespeeds and fluid overpressure in a region of shallow geodetic locking and slow slip, Hikurangi subduction margin, New Zealand. Earth Planet. Sci. Lett. 389, 1–13. https://doi.org/10.1016/j. epsl.2013.12.021.
- Chesley, C., Naif, S., Key, K., Bassett, D., 2021. Fluid-rich subducting topography generates anomalous forearc porosity. Nature 595 (7866), 255–260. https://doi.org/ 10.1038/s41586-021-03619-8.
- Cordell, D., Naif, S., Evans, R., Key, K., Constable, S., Shillington, D., Bécel, A., 2023. Forearc seismogenesis in a weakly coupled subduction zone influenced by slab mantle fluids. Nat. Geosci. https://doi.org/10.1038/s41561-023-01260-w.
- Cross, R.S., Freymueller, J.T., 2008. Evidence for and implications of a Bering plate based on geodetic measurements from the aleutians and western Alaska. J. Geophys. Res. 113 (B7), B07405. https://doi.org/10.1029/2007jb005136.
- Davies, J., Sykes, L., House, L., Jacob, K., 1981. Shumagin seismic gap, alaska peninsula: history of great earthquakes, tectonic setting, and evidence for high seismic potential. J. Geophys. Res. 86 (B5), 3821–3855. https://doi.org/10.1029/ JB086iB05p03821.
- Delph, J.R., Levander, A., Niu, F., 2018. Fluid controls on the heterogeneous seismic characteristics of the Cascadia margin. Geophys. Res. Lett. 45 (20), 11. https://doi. org/10.1029/2018 gl079518, 021-011,029.
- Drooff, C., Freymueller, J.T., 2021. New constraints on slip deficit on the aleutian megathrust and inflation at Mt. Veniaminof, Alaska from repeat GPS measurements. Geophys. Res. Lett. 48 (4) https://doi.org/10.1029/2020 gl091787 e2020GL091787
- Egbert, G.D., Yang, B., Bedrosian, P.A., Key, K., Livelybrooks, D.W., Schultz, A., Kelbert, A., Parris, B., 2022. Fluid transport and storage in the Cascadia forearc influenced by overriding plate lithology. Nat. Geosci. 15 (8), 677–682. https://doi. org/10.1038/s41561-022-00981-8.
- Ekström, G., Nettles, M., Dziewoński, A.M., 2012. The global CMT project 2004–2010: centroid-moment tensors for 13,017 earthquakes. Phys. Earth Planet. Inter. 200-201, 1–9. https://doi.org/10.1016/j.pepi.2012.04.002.
- Elliott, J., Freymueller, J.T., 2020. A block model of present-day kinematics of Alaska and western Canada. J. Geophys. Res. Solid Earth 125 (7), e2019JB018378. https:// doi.org/10.1029/2019jb018378.
- Elliott, J.L., Grapenthin, R., Parameswaran, R.M., Xiao, Z., Freymueller, J.T., Fusso, L., 2022. Cascading rupture of a megathrust. Sci. Adv. 8 (18), eabm4131. https://doi. org/10.1126/sciadv.abm4131.
- Fletcher, H.J., Freymueller, J.T., 2003. New constraints on the motion of the Fairweather fault, Alaska, from GPS observations. Geophys. Res. Lett. 30 (3), 1139. https://doi. org/10.1029/2002 gl016476.
- Freymueller, J.T., Suleimani, E.N., Nicolsky, D.J., 2021. Constraints on the slip distribution of the 1938 Mw 8.3 Alaska Peninsula earthquake from tsunami

- modeling. Geophys. Res. Lett. 48 (9), e2021GL092812 https://doi.org/10.1029/
- Gou, T., Xia, S., Huang, Z., Zhao, D., 2022. Structural heterogeneity of the Alaska-Aleutian forearc: implications for interplate coupling and seismogenic behaviors. J. Geophys. Res. Solid Earth 127 (11), e2022JB024621. https://doi.org/10.1029/2022jb024621
- Guo, H., McGuire, J.J., Zhang, H., 2021. Correlation of porosity variations and rheological transitions on the southern Cascadia megathrust. Nat. Geosci. 14 (5), 341–348. https://doi.org/10.1038/s41561-021-00740-1.
- Guo, H., Zhang, H., Froment, B., 2018. Structural control on earthquake behaviors revealed by high-resolution Vp/Vs imaging along the Gofar transform fault, East Pacific Rise. Earth Planet. Sci. Lett. 499, 243–255. https://doi.org/10.1016/j. ensl 2018 07 037
- Hayes, G.P., Moore, G.L.P., Daniel, E., Hearne, M.F., Hanna, Furtney, M.S., Gregory, M., 2018. Slab2, a comprehensive subduction zone geometry model. Science 362 (6410), 58–61. https://doi.org/10.1126/science.aat4723.
- He, B., Wei, X., Wei, M., Shen, Y., Alvarez, M., Schwartz, S.Y., 2023. A shallow slow slip event in 2018 in the Semidi segment of the Alaska subduction zone detected by machine learning. Earth Planet. Sci. Lett. 612, 118154 https://doi.org/10.1016/j. epsl 2023 118154
- Heise, W., Caldwell, T.G., Bannister, S., Bertrand, E.A., Ogawa, Y., Bennie, S.L., Ichihara, H., 2017. Mapping subduction interface coupling using magnetotellurics: hikurangi margin, New Zealand. Geophys. Res. Lett. 44 (18), 9261–9266. https://doi.org/10.1002/2017 gl074641.
- Henrys, S., Eberhart-Phillips, D., Bassett, D., Sutherland, R., Okaya, D., Savage, M., Evanzia, D., Stern, T., Sato, H., Mochizuki, K., Iwasaki, T., Kurashimo, E., Seward, A., Wech, A., 2020. Upper plate heterogeneity along the southern Hikurangi margin. New Zealand. Geophys. Res. Lett. 47 (4), e2019GL085511 https://doi.org/10.1029/2019 gl085511.
- Holt, A.F., Condit, C.B., 2021. Slab temperature evolution over the lifetime of a subduction zone. Geochem. Geophys. Geosyst. 22 (6), e2020GC009476 https://doi. org/10.1029/2020 gc009476.
- Holtkamp, S.G., 2017. Slow Slip and Mixed Seismic/Aseismic Moment Release Episodes on the Alaskan-Aleutian Megathrust. EarthScope National Meeting, Anchorage, Alaska.
- Horowitz, W.L., Steffy, D.A., Hoose, P.J., Turner, R.F., 1989. Geologic Report For the Shumagin Planning Area, Western Gulf of Alaska. U.S. Department of the Interior, Minerals Management Service, Alaska OCS Region., OCS Report, MMS 89-0097.
- Ikari, M.J., Saffer, D.M., Marone, C., 2009. Frictional and hydrologic properties of clayrich fault gouge. J. Geophys. Res. 114 (B5) https://doi.org/10.1029/2008jb006089.
- Jarrard, R.D., 1986. Relations among subduction parameters. Rev. Geophys. 24 (2), 217–284. https://doi.org/10.1029/RG024i002p00217.
- Jiang, Y., González, P.J., Bürgmann, R., 2022. Subduction earthquakes controlled by incoming plate geometry: the 2020 M>7.5 Shumagin, Alaska, earthquake doublet. Earth Planet. Sci. Lett. 584 https://doi.org/10.1016/j.epsl.2022.117447.
- Earth Planet. Sci. Lett. 584 https://doi.org/10.1016/j.epsl.2022.117447.

  Katayama, I., Kubo, T., Sakuma, H., Kawai, K., 2015. Can clay minerals account for the behavior of non-asperity on the subducting plate interface? Prog. Earth Planet. Sci 2 (30). https://doi.org/10.1186/s40645-015-0063-4
- Kodaira, S., Iidaka, T., Kato, A., Park, J.O., Iwasaki, T., Kaneda, Y., 2004. High pore fluid pressure may cause silent slip in the Nankai Trough. Science 304 (5678), 1295–1298. https://doi.org/10.1126/science.1096535.
- Kuehn, H., 2019. Along-trench Segmentation and Down-Dip Limit of the Seismogenic Zone At the Eastern Alaska-Aleutian subduction Zone. Dalhousie University, p. 334.
- Lay, T., Kanamori, H., Ammon, C.J., Koper, K.D., Hutko, A.R., Ye, L., Yue, H., Rushing, T. M., 2012. Depth-varying rupture properties of subduction zone megathrust faults. J. Geophys. Res. 117 (B04311), B04311. https://doi.org/10.1029/2011jb009133.
- Li, J., Shillington, D.J., Bécel, A., Nedimović, M.R., Webb, S.C., Saffer, D.M., Keranen, K. M., Kuehn, H., 2015. Downdip variations in seismic reflection character: Implications for fault structure and seismogenic behavior in the Alaska subduction zone. J. Geophys. Res. Solid Earth 120, 7883–7904. https://doi.org/10.1002/2015.JR012338
- Li, J., Shillington, D.J., Saffer, D.M., Bécel, A., Nedimović, M.R., Kuehn, H., Webb, S.C., Keranen, K.M., Abers, G.A., 2018a. Connections between subducted sediment, porefluid pressure, and earthquake behavior along the Alaska megathrust. Geology 46 (4), 299–302. https://doi.org/10.1130/g39557.1.
- Li, S., Freymueller, J.T., 2018. Spatial variation of slip behavior beneath the Alaska Peninsula along Alaska-Aleutian subduction zone. Geophys. Res. Lett 45 (8), 3453–3460. https://doi.org/10.1002/2017gl076761.
- Li, S., Freymueller, J., McCaffrey, R., 2016. Slow slip events and time-dependent variations in locking beneath Lower Cook Inlet of the Alaska-Aleutian subduction zone. J. Geophys. Res. Solid Earth 121 (2), 1060–1079. https://doi.org/10.1002/ 2015jb012491.
- Li, Z., Wiens, D.A., Shen, W., Shillington, D.J., 2024. Along-strike variations of Alaska subduction zone structure and hydration determined from amphibious seismic data. J. Geophys. Res. Solid Earth, e2023JB027800. https://doi.org/10.1029/ 2023JB027800
- Lindsey, E.O., Mallick, R., Hubbard, J.A., Bradley, K.E., Almeida, R.V., Moore, J.D.P., Bürgmann, R., Hill, E.M., 2021. Slip rate deficit and earthquake potential on shallow megathrusts. Nat. Geosci. 14 (5), 321–326. https://doi.org/10.1038/s41561-021-00736-x.
- Liu, C., Lay, T., Xiong, X., 2022a. The 29 july 2021 M<sub>w</sub> 8.2 chignik, Alaska Peninsula earthquake rupture inferred from seismic and geodetic observations: *re*-rupture of the western 2/3 of the 1938 rupture zone. Geophys. Res. Lett. 49 (4) https://doi.org/10.1029/2021 el096004.
- Liu, C., Zhang, S., Sheehan, A.F., Ritzwoller, M.H., 2022b. Surface wave isotropic and azimuthally anisotropic dispersion across Alaska and the Alaska-Aleutian subduction

- zone. J. Geophys. Res. Solid Earth 127 (11), e2022JB024885. https://doi.org/10.1029/2022ib024885.
- Lynner, C., 2021. Anisotropy-revealed change in hydration along the Alaska subduction zone. Geology 49 (9), 1122–1125. https://doi.org/10.1130/g48860.1.
- McCaffrey, R., 2002. Crustal block rotations and plate coupling. In: Stein, S.A., Freymueller, J.T. (Eds.), Plate Boundary Zones, AGU Geodynamics Series. AGU, Washington, D.C, pp. 101–122.
- Meyer, B., Chulliat, A., Saltus, R., 2017. Derivation and error analysis of the earth magnetic anomaly grid at 2 " resolution version 3 (EMAG2v3). Geochem. Geophys. Geosyst. 18 (12), 4522–4537. https://doi.org/10.1002/2017 gc007280.
- Molina-Ormazabal, D., Ampuero, J.P., Tassara, A., 2023. Diverse slip behavior of velocity-weakening fault barriers. Nat. Geosci. 16 (12), 1200–1207. https://doi.org/ 10.1038/s41561-023-01312-1.
- Moreno, M., Haberland, C., Oncken, O., Rietbrock, A., Angiboust, S., Heidbach, O., 2014. Locking of the Chile subduction zone controlled by fluid pressure before the 2010 earthquake. Nat. Geosci. 7 (4), 292–296. https://doi.org/10.1038/ngeo2102.
- Nishikawa, T., Matsuzawa, T., Ohta, K., Uchida, N., Nishimura, T., Ide, S., 2019. The slow earthquake spectrum in the Japan Trench illuminated by the S-net seafloor observatories. Science 365 (6455), 808–813. https://doi.org/10.1126/science.
- Okada, Y., 1992. Internal deformation due to shear and tensile faults in a half-space. Bull. Seismol. Soc. Am. 82 (2), 1018–1040. https://doi.org/10.1785/BSSA0820021018.
- Onyango, E.A., Worthington, L.L., Schmandt, B., Abers, G.A., 2022. Subduction zone interface structure within the southern M<sub>W</sub> 9.2 1964 great Alaska earthquake asperity: constraints from receiver functions across a spatially dense node array. Geophys. Res. Lett. 49 (15), e2022GL098334 https://doi.org/10.1029/2022gl098334.
- Pesicek, J.D., Zhang, H., Thurber, C.H., 2014. Multiscale Seismic tomography and earthquake relocation incorporating differential time data: application to the maule subduction zone, Chile. Bull. Seismol. Soc. Am. 104 (2), 1037–1044. https://doi.org/ 10.1285/0120130121
- Plafker, G., Moore, J.C., Winkler, G.R., Plafker, G., Berg, H.C., 1994. Geology of the Southern Alaska margin, The Geology of Alaska. Geological Society of America, p. 0.
- Reece, R.S., Gulick, S.P.S., Christeson, G.L., Horton, B.K., van Avendonk, H., Barth, G., 2013. The role of farfield tectonic stress in oceanic intraplate deformation, Gulf of Alaska. J. Geophys. Res. Solid Earth 118 (5), 1862–1872. https://doi.org/10.1002/ igrb.50177.
- Ruppert, N.A., Barcheck, G., Abers, G.A., 2022. Enhanced regional earthquake catalog with alaska amphibious community seismic experiment data. Seismol. Res. Lett. 94 (1), 522–530. https://doi.org/10.1785/0220220226.
- Saffer, D.M., Tobin, H.J., 2011. Hydrogeology and mechanics of subduction zone forearcs: fluid flow and pore pressure. Annu. Rev. Earth Planet. Sci. 39 (1), 157–186. https://doi.org/10.1146/annurey-earth-040610-133408.
- Sallares, V., Ranero, C.R., 2019. Upper-plate rigidity determines depth-varying rupture behaviour of megathrust earthquakes. Nature 576 (7785), 96–101. https://doi.org/ 10.1038/s41586-019-1784-0.
- Shillington, D.J., Bécel, A., Nedimović, M.R., 2022. Upper plate structure and megathrust properties in the Shumagin Gap near the July 2020 M7.8 Simeonof event. Geophys. Res. Lett. 49 (2), e2021GL096974 https://doi.org/10.1029/2021 gl096974.
- Shillington, D.J., Bécel, A., Nedimović, M.R., Kuehn, H., Webb, S.C., Abers, G.A., Keranen, K.M., Li, J., Delescluse, M., Mattei-Salicrup, G.A., 2015. Link between plate fabric, hydration and subduction zone seismicity in Alaska. Nat. Geosci. 8 (12), 961–964. https://doi.org/10.1038/ngeo2586.
- Suito, H., Freymueller, J.T., 2009. A viscoelastic and afterslip postseismic deformation model for the 1964 Alaska earthquake. J. Geophys. Res. Solid Earth 114 (B11), B11404. https://doi.org/10.1029/2008jb005954.
- Sun, T., Saffer, D., Ellis, S., 2020. Mechanical and hydrological effects of seamount subduction on megathrust stress and slip. Nat. Geosci. 13 (3), 249–255. https://doi. org/10.1038/s41561-020-0542-0.
- Takei, Y., 2002. Effect of pore geometry on V<sub>P</sub>/V<sub>S</sub>: from equilibrium geometry to crack. J. Geophys. Res. 107 (B2) https://doi.org/10.1029/2001jb000522. ECV-6.
- Tobin, H.J., Saffer, D.M., 2009. Elevated fluid pressure and extreme mechanical weakness of a plate boundary thrust, Nankai Trough subduction zone. Geology 37 (8), 679–682. https://doi.org/10.1130/g25752a.1.
- von Huene, R., Miller, J.J., Krabbenhoeft, A., 2021. The Alaska convergent margin backstop splay fault zone, a potential large tsunami generator between the frontal prism and continental framework. Geochem. Geophys. Geosyst. 22 (1), e2019GC008901 https://doi.org/10.1029/2019 gc008901.
- von Huene, R., Miller, J.J., Weinrebe, W., 2012. Subducting plate geology in three great earthquake ruptures of the western Alaska margin, Kodiak to Unimak. Geosphere 8 (3), 628–644. https://doi.org/10.1130/ges00715.1.
- Vrolijk, P., 1987. Tectonically driven fluid flow in the Kodiak accretionary complex, Alaska. Geology 15 (5), 466–469. https://doi.org/10.1130/0091-7613(1987) 15<466:TDFFIT>2.0.CO;2.
- Wang, K., Wells, R., Mazzotti, S., Hyndman, R.D., Sagiya, T., 2003. A revised dislocation model of interseismic deformation of the Cascadia subduction zone. J. Geophys. Res. Solid Earth 108 (B1). https://doi.org/10.1029/2001jb001227.
- Wei, S.S., Ruprecht, P., Gable, S.L., Huggins, E.G., Ruppert, N., Gao, L., Zhang, H., 2021. Along-strike variations in intermediate-depth seismicity and arc magmatism along the Alaska Peninsula. Earth Planet. Sci. Lett. 563, 116878 https://doi.org/10.1016/j. epsl 2021 116878
- Witter, R.C., Briggs, R.W., Engelhart, S.E., Gelfenbaum, G., Koehler, R.D., Barnhart, W. D., 2014. Little late holocene strain accumulation and release on the aleutian megathrust below the Shumagin Islands, Alaska. Geophys. Res. Lett 41 (7), 2359–2367. https://doi.org/10.1002/2014 gl059393.

- Xiao, Z., Freymueller, J.T., Grapenthin, R., Elliott, J.L., Drooff, C., Fusso, L., 2021. The deep Shumagin gap filled: kinematic rupture model and slip budget analysis of the 2020 Mw 7.8 Simeonof earthquake constrained by GNSS, global seismic waveforms, and floating InSAR. Earth Planet. Sci. Lett. 576, 117241 https://doi.org/10.1016/j. epsl.2021.117241.
- Ye, L., Lay, T., Kanamori, H., Yamazaki, Y., Cheung, K.F., 2021. The 22 july 2020M 7.8 shumagin seismic gap earthquake: partial rupture of a weakly coupled megathrust. Earth Planet. Sci. Lett 562, 116879. https://doi.org/10.1016/j.epsl.2021.116879.
- Zelt, C.A., 1998. Lateral velocity resolution from three-dimensional seismic refraction data. Geophys. J. Int. 135 (3), 1101–1112. https://doi.org/10.1046/j.1365-246X 1998 00695 x
- Zhang, H., Thurber, C.H., 2003. Double-difference tomography: the method and its application to the Hayward fault, California. Bull. Seismol. Soc. Am. 93 (5), 1875–1889. https://doi.org/10.1785/0120020190.
- Zhao, B., Burgmann, R., Wang, D., Zhang, J., Yu, J., Li, Q., 2022a. Aseismic slip and recent ruptures of persistent asperities along the Alaska-Aleutian subduction zone. Nat. Commun. 13 (1), 3098. https://doi.org/10.1038/s41467-022-30883-7.
- Zhao, D., Katayama, Y., Toyokuni, G., 2022b. The Moho, slab and tomography of the East Japan forearc derived from seafloor S-net data. Tectonophysics 837, 229452. https://doi.org/10.1016/j.tecto.2022.229452.